Effects of Hierarchical Architecture on Electronic and Mechanical Properties of Nanocast Monolithic Porous Carbons and Carbon−Carbon Nanocomposites

Zhiyong Wang, Fan Li, Nicholas S. Ergang, and Andreas Stein*

Department of Chemistry, University of Minnesota, Minneapolis, Minnesota 55455

Received August 29, 2006. Revised Manuscript Received September 5, 2006

This study compares the effects of meso- and macroporosity and the influence of nanocomposite structure on textural, electronic, and mechanical properties of monolithic carbon samples. Glassy carbon monoliths with three-dimensionally ordered macropores and walls containing mesopores (3DOM/m C) were synthesized by nanocasting from monolithic silica with hierarchical pore structure. The porous silica monoliths (3DOM/m SiO_2) were prepared by combining colloidal crystal templating with surfactant templating. These preforms were infiltrated with a phenolic resin through a gas-phase process. After carbonization and HF extraction of silica, the resulting carbon monoliths maintained the open, interconnected macropore structure of the preform and the mesoporosity of the skeleton, which provided a high surface area >1200 m^2/g to the material. Subsequent introduction of more graphitic, nitrogen-doped carbon into the mesopores by chemical vapor deposition produced a monolithic nanocomposite material (3DOM/m C/C). The materials were characterized in detail by powder X-ray diffraction, Raman spectroscopy, small-angle X-ray scattering, scanning electron microscopy, transmission electron microscopy, X-ray photoelectron spectroscopy, thermogravimetric analysis, nitrogen-adsorption measurements, depth-sensing indentation, and electrochemical measurements. The mechanical strength, electronic conductivity, and capacity for lithiation of 3DOM/m C, 3DOM/m C/C, and a 3DOM carbon prepared from resorcinol-formaldehyde precursors without templated mesopores (3DOM RFC) were compared to evaluate the effects of the wall nanostructure and composition on these properties. The mechanical strength and electronic conductivity of the nanocomposite were significantly higher than those before addition of the second carbon phase. The nanocomposite suppressed formation of a solid-electrolyte interface layer during lithiation and had higher lithiation capacity than 3DOM RFC at high discharge rates, but not at low rates.

Introduction

Porous carbon materials enjoy widespread use in applications as sorbents, filters, catalysts and catalyst supports, electrodes, sensors, electrochemical double-layer capacitors, rechargeable lithium batteries, hydrogen storage systems, and many other applications.[1,2] In recent years new synthetic methods have been developed to prepare glassy and graphitic carbon structures with designed porosities and architectures. With use of hard and soft templates, microporous, mesoporous, or macroporous carbon can be synthesized with either periodic or disordered pore structures. When multiple templating techniques are employed, hierarchical pore structuring is also possible. For these novel carbon architectures to be introduced into applications, it is important to understand the effects of carbon architecture on materials properties, including surface area, mechanical strength, electrical conductivity, and for lithium battery applications, their ability to intercalate lithium. Furthermore, these properties should be tunable through the materials synthesis to optimize them for a particular application. In this study, we used colloidal crystal templating, nanocasting, and chemical vapor deposition methods to prepare porous carbon with periodic arrays of macropores (three-dimensionally ordered macroporous carbon or 3DOM carbon), where amorphous carbon walls contained either adventitious micropores, templated open mesopores, or graphite-filled mesopores to produce a novel carbon/carbon nanocomposite. The structures and texture of these materials were characterized in detail and related to mechanical and electronic properties. This work demonstrates that these properties can be readily manipulated by modifying the carbon architecture and composition.

The basic structure of all the materials in this work is derived from colloidal crystal templating methods that produce 3DOM materials or inverse opals. These are of interest for their potential applications as photonic crystals,[3−6] separation and filtration agents,[7,8] catalyst supports,[9] and

* To whom correspondence should be addressed. E-mail: stein@chem.umn.edu.

(1) Ryoo, R.; Joo, S. H.; Kruk, M.; Jaroniec, M. *Adv. Mater.* **2001**, *13*, 677−681.
(2) Yang, H.; Zhao, D. *J. Mater. Chem.* **2005**, *15*, 1217−1231.
(3) Lodahl, P.; van Driel, A. F.; Nikolaev, I. S.; Irman, A.; Overgaag, K.; Vanmaekelbergh, D.; Vos, W. L. *Nature* **2004**, *430*, 654−657.
(4) Blanco, A.; Chomski, E.; Grabtchak, S.; Ibisate, M.; John, S.; Leonardo, S. W.; Lopez, C.; Meseguer, F.; Miguez, H.; Mondia, J. P.; Ozin, G. A.; Toader, O.; Van Driel, H. M. *Nature* **2000**, *405*, 437−440.
(5) Tetreault, N.; Miguez, H.; Ozin, G. A. *Adv. Mater.* **2004**, *16*, 1471−1476.
(6) Norris, D. J.; Vlasov, Y. A. *Adv. Mater.* **2001**, *13*, 371−376 and references therein.

10.1021/cm062050u CCC: $33.50
Published on Web 10/12/2006

electrode materials for batteries[10−14] or fuel cells.[15] To prepare 3DOM materials, a colloidal crystal composed of close-packed, monodisperse polymer or silica spheres is infiltrated with a fluid precursor and processed to form a bicontinuous wall/macropore structure after template removal. The walls in inverse opal structures have typical thicknesses of tens of nanometers, and pore diameters are hundreds of nanometers. While it is difficult to form monolithic inverse opals for many compositions, 3DOM silica and carbon can be prepared as monoliths with dimensions of millimeters to centimeters.[10]

Secondary pore structures can be introduced into the macropore walls by an appropriate choice of synthetic methods. Adventitious micropores and/or mesopores are often formed in 3DOM silica or 3DOM carbon during sol−gel processing.[10,16] More controlled mesopores can be introduced by surfactant-, liquid-crystal-, or block-copolymer templating.[15,17−20] For silica systems, such syntheses are now well-established. Recently, direct triblock copolymer templating has also been extended to ordered mesoporous carbon powders, films, and monoliths with phenolic resin as a carbon source.[21−26] However, the synthesis of hierarchically structured meso-/macroporous carbon monoliths by direct surfactant templating within a colloidal crystal remains a challenge. Alternatively, nanocasting techniques can be employed in which mesoporous preforms of various mesostructures are filled with carbon or silica precursors and processed to leave replica structures.[1,27−30] Nanocasting from mesoporous silica monoliths permits the formation of mesoporous carbon monoliths with various morphologies, such as hexagonal *p6mm*[31] and bicontinuous cubic *Ia3d* symmetries.[2,32] By combining multiple templating techniques, it is possible to form carbon with hierarchical pore structures. Carbon monoliths with bimodal pores and even trimodal pores were reported recently, including carbon materials with ordered, uniform macropores and mesopores.[15,33−37]

In applications that rely on porous carbon as a structural, reactive, or electronic component, the crystallographic phase of carbon plays an important role. With increasing graphitic character, the electronic conductivity of carbon can be raised, but the carbon also becomes softer.[38,39] Phenol−formaldehyde (PF) or resorcinol−formaldehyde (RF) precursors produce nongraphitizable, hard carbons. The skeleton of mesoporous carbon produced from these precursors is amorphous, similar to the case of mesoporous silica. In the same way, monolithic 3DOM carbon obtained from RF polymer precursors and employed as an electrode for lithium batteries was mainly amorphous.[10] Ordered mesoporous carbon powders with highly graphitic pore walls were synthesized by Ryoo and co-workers from an SBA-15 mold with acenaphthene as carbon precursor.[40] Schueth and co-workers described a vapor-phase oxidative polymerization technique for the synthesis of ordered mesoporous carbon with pyrrole as carbon precursor and mesoporous silica as hard template, which showed some graphitic order.[41] Inverse opals with graphitic content can be synthesized by high-temperature reactions.[42]

Here we explore a new strategy to vary the graphitic content in an inverse opal carbon material, modify wall thicknesses, porosities, and surface areas, and alter the mechanical strength, conductivity, and lithium ion capacity of porous carbon monoliths: the fabrication of macroporous glassy carbon/amorphous carbon nanocomposites. The first step in this multistep procedure involves the synthesis of monolithic silica with hierarchical porosity (three-dimensionally ordered macroporous/mesoporous silica, 3DOM/m SiO_2) using poly(methyl methacrylate) (PMMA) colloidal crystals as templates for macropores[43] and silicate/poly(oxyethylene)

(7) Nakanishi, K. M.; Soga, N.; Tanaka, N. *J. Sol-Gel Sci. Technol.* **1998**, *13*, 163−169.
(8) Sarrade, S. J.; Rios, G. M.; Carles, M. *Sep. Purif. Technol.* **1998**, *14*, 19−25.
(9) Diddams, P. *Inorganic Supports and Catalysts*; Smith, K. Ed.; Ellis Horwood: New York, 1992; pp 3−39.
(10) Lee, K. T.; Lytle, J. C.; Ergang, N. S.; Oh, S. M.; Stein, A. *Adv. Funct. Mater.* **2005**, *15*, 547−556.
(11) Ergang, N. S.; Lytle, J. C.; Yan, H.; Stein, A. *J. Electrochem. Soc.* **2005**, *152*, A1989−A1995.
(12) Sorensen, E. M.; Barry, S. J.; Jung, H.-K.; Rondinelli, J. M.; Vaughey, J. T.; Poeppelmeier, K. R. *Chem. Mater.* **2006**, *18*, 482−489.
(13) Long, J. W.; Dunn, B.; Rolison, D. R.; White, H. S. *Chem. Rev.* **2004**, *104*, 4463−4492.
(14) Ergang, N. S.; Lytle, J. C.; Lee, K. T.; Oh, S. M.; Smyrl, W. H.; Stein, A. *Adv. Mater.* **2006**, *18*, 1750−1753.
(15) Chai, G. S.; Shin, I. S.; Jong-Sung, Y. *Adv. Mater.* **2004**, *16*, 2057−2061.
(16) Holland, B. T.; Blanford, C. F.; Do, T.; Stein, A. *Chem. Mater.* **1999**, *11*, 795−805.
(17) Yang, P.; Deng, T.; Zhao, D.; Feng, P.; Pine, D.; Chmelka, B. F.; Whitesides, G. M.; Stucky, G. D. *Science* **1998**, *282*, 2244−2247.
(18) Villaescusa, L. A.; Mihi, A.; Rodriguez, I.; Garcia-Bennett, A. E.; Miguez, H. *J. Phys. Chem. B* **2005**, *109*, 19643−19649.
(19) Sel, O.; Kuang, D.; Thommes, M.; Smarsly, B. *Langmuir* **2006**, *22*, 2311−2322.
(20) Oh, C.-G.; Baek, Y.; Ihm, S.-K. *Adv. Mater.* **2005**, *17*, 270−273.
(21) Tanaka, S.; Nishiyama, N.; Egashira, Y.; Ueyama, K. *Chem. Commun.* **2005**, 2125−2127.
(22) Meng, Y.; Gu, D.; Zhang, F.; Shi, Y.; Yang, H.; Li, Z.; Yu, C.; Tu, B.; Zhao, D. *Angew. Chem., Int. Ed.* **2005**, *44*, 2−8.
(23) Zhang, F.; Meng, Y.; Gu, D.; Yan, Y.; Yu, C.; Tu, B.; Zhao, D. *J. Am. Chem. Soc.* **2005**, *127*, 13508−13509.
(24) Liang, C. D.; Hong, K. L.; Guiochon, G. A.; Mays, J. W.; Dai, S. *Angew. Chem., Int. Ed.* **2004**, *43*, 5785−5789.
(25) Kosonen, H.; Valkama, S.; Nykanen, A.; Toivanen, M.; Brinke, G. T.; Ruokolainen, J.; Ikkala, O. *Adv. Mater.* **2006**, *18*, 201−205.
(26) Liang, C.; Dai, S. *J. Am. Chem. Soc.* **2006**, *128*, 5316−5317.
(27) Joo, S. H.; Choi, S. J.; Oh, I.; Kwak, J.; Liu, Z.; Terasaki, O.; Ryoo, R. *Nature* **2001**, *412*, 169−172.
(28) Ryoo, R.; Joo, S. H.; Jun, S. *J. Phys. Chem. B* **1999**, *103*, 7743−7746.
(29) Jun, S.; Joo, S. H.; Ryoo, R.; Kruk, M.; Jaroniec, M.; Liu, Z.; Ohsuna, T.; Terasaki, O. *J. Am. Chem. Soc.* **2000**, *122*, 10712−10713.
(30) Zhou, H.; Zhu, S.; Hibino, M.; Honma, I.; Ichihara, M. *Adv. Mater.* **2003**, *15*, 2107−2111.
(31) Wang, L.; Lin, S.; Lin, K.; Yin, C.; Liang, D.; Di, Y.; Fan, P.; Jiang, D.; Xiao, F. *Microporous Mesoporous Mater.* **2005**, *85*, 136−142.
(32) Yang, H.; Shi, Q.; Liu, X.; Xie, S.; Jiang, D.; Zhang, F.; Yu, C.; Tu, B.; Zhao, D. *Chem. Commun.* **2002**, 2842−2843.
(33) Taguchi, A.; Smatt, J.-H.; Linden, M. *Adv. Mater.* **2003**, *15*, 1209−1211.
(34) Alvarez, S.; Esquena, J.; Solans, C.; Fuertes, A. B. *Adv. Eng. Mater.* **2004**, *6*, 897−899.
(35) Shi, Z.-G.; Feng, Y.-Q.; Xu, L.; Da, S.-L.; Zhang, M. *Carbon* **2003**, *41*, 2677−2679.
(36) Lu, A.-H.; Smatt, J.-H.; Linden, M. *Adv. Funct. Mater.* **2005**, *15*, 865−871.
(37) Yuan, Z.-Y.; Su, B.-L. *J. Mater. Chem.* **2006**, *16*, 663−677.
(38) Marx, D. T.; Riester, L. *Carbon* **1999**, *37*, 1679−1684.
(39) Welch, B. J. *Adv. Sci. Technol.* **1999**, *16*, 647−659.
(40) Kim, T.-W.; Park, I.-S.; Ryoo, R. *Angew. Chem., Int. Ed.* **2003**, *42*, 4375−4379.
(41) Yang, C. M.; Weidenthaler, C.; Spliethoff, B.; Mayanna, M.; Schueth, F. *Chem. Mater.* **2005**, *17*, 355−358.
(42) Zakhidov, A. A.; Baughman, R. H.; Iqbal, Z.; Cui, C.; Khayrullin, I.; Dantas, S. O.; Marti, J.; Ralchenko, V. G. *Science* **1998**, *282*, 897−901.
(43) Holland, B. T.; Blanford, C. F.; Stein, A. *Science* **1998**, *281*, 538−540.

Scheme 1. Diagram of the Synthesis of 3DOM/m Nanocomposite Monoliths[a]

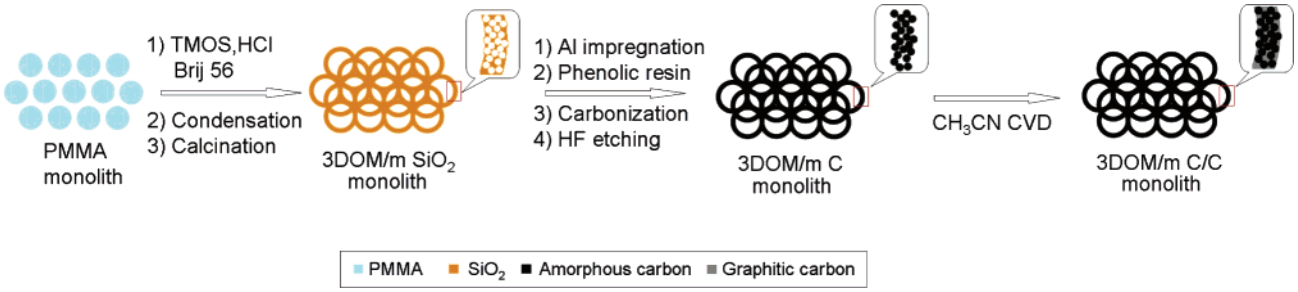

[a] PMMA colloidal crystal monoliths were used as the starting template. After infiltration with a silica source and a meso-structure-directing agent, followed by condensation of silica and calcination to remove PMMA, 3DOM/m SiO_2 monoliths were obtained. Acidic sites to catalyze polymer formation were added by aluminum impregnation. Mesopores in 3DOM/m SiO_2 were then filled with phenol−formaldehyde polymer via a gas-phase process. 3DOM/m carbon monoliths, which are replicas of 3DOM/m SiO_2, were produced by carbonization of the silica/polymer composite, followed by HF etching of silica. CVD within these 3DOM/m C monoliths using acetonitrile as a precursor yielded the final product: a 3DOM/m amorphous carbon/graphitic carbon nanocomposite.

surfactant solutions as precursors for mesoporous walls.[44,45] After calcination, the PMMA and surfactant templates were removed and a 3DOM/m SiO_2 was produced. This biporous silica monolith was employed as a hard template to prepare its carbon replica by gas-phase polymerization, carbonization, and hydrofluoric acid etching to remove the silica. This material with open mesopores and macropores was denoted 3DOM/m C. In a final step, N-doped graphite was introduced into the mesopores by chemical vapor deposition (CVD) with acetonitrile as a precursor. CVD had previously been used to fabricate amorphous and graphitic mesoporous carbon, hollow spheres, nanorods and nanotubules, and zeolite replicas with various carbon precursors, such as propylene, styrene, benzene, and acetonitrile.[46−52] In the nanocasting and mesopore-filling steps used in this study, gas-phase polymerization and CVD are better choices over liquid impregnation methods because phenolic resin and graphitic carbon can be deposited mostly inside mesopores (if the reaction time is controlled), while macropores and their connections are left unaffected. Moreover, the coating thickness on the macropore walls is controllable simply by varying the CVD time. The resulting monolithic carbon/carbon nanocomposites are denoted 3DOM/m C/C. The overall process is summarized in Scheme 1. To the best of our knowledge, carbon monoliths with ordered macropores and nanocomposite walls composed of mixed carbon phases have not been reported. These materials offer an opportunity to tune and optimize carbon properties for specific applications.

The materials were characterized in detail by powder X-ray diffraction (XRD), Raman spectroscopy, small-angle X-ray scattering (SAXS), scanning electron microscopy (SEM), transmission electron microscopy (TEM), X-ray photoelectron spectroscopy (XPS), thermogravimetric analysis (TGA), nitrogen-adsorption measurements, depth-sensing indentation (DSI), and electrochemical measurements. The mechanical strength, electronic conductivity, and capacity for lithiation of 3DOM/m C, 3DOM/m C/C, and a 3DOM carbon prepared from resorcinol-formaldehyde precursors without templated mesopores (3DOM RFC) were compared to evaluate the effects of the wall nanostructure and composition on these properties. An understanding of the relationships between synthesis, structure, mechanical properties, and electrochemical behavior is important for applications that would require robust, conductive, porous monoliths, including lithium-ion batteries,[14] sensors, electrocatalytic systems, fuel cells, and supercapacitors.

Experimental Section

Chemicals. Chemicals used in this experiment were obtained from the following sources: 2,2′-azobis(2-methyl propionamidine) dihydrochloride (AMPD) initiator (97%), methyl methacrylate monomer (MMA) (99%), tetramethyl orthosilicate (TMOS), Brij 56, paraformaldehyde (95%), and resorcinol (99%) were purchased from Aldrich. Aluminum trichloride hexahydrate, sodium carbonate, phenol (ACS reagent), and formaldehyde (37% aqueous solution) were from Fisher Scientific. Hydrochloric acid (37%), hydrofluoric acid (48%), and acetonitrile were from Mallinckrodt Chemicals.

Synthesis of PMMA Colloidal Crystal Template. In this study, PMMA spheres were prepared by emulsifier-free emulsion polymerization of MMA at 70 °C with AMPD as an initiator, as described elsewhere.[53] The resulting PMMA sphere suspension was transferred to a glass crystallization dish and stored for several weeks at room temperature without agitation. After the evaporation of water, PMMA spheres deposited on the bottom of the container, forming opalescent colloidal crystal pieces. These pieces were used as templates in syntheses of macro-/mesoporous silica and 3DOM RFC monoliths.

Synthesis of 3DOM/m SiO_2 Monoliths. In a typical synthesis, 2 g of Brij 56 was mixed with 4 g of TMOS and stirred at 45 °C until a homogeneous phase was formed. Then 2 g of 0.05 M HCl was added, and the mixture was stirred vigorously for 5 min. The hydrolysis of TMOS was accompanied by a brief rise in temperature. Then 5−8 pieces of the PMMA template (ca. 1 cm^3/piece) were placed in a vial. The acidified mixture of Brij 56 and TMOS was added until the template pieces were approximately half-immersed in the precursor. When the liquid mixture came in contact with the PMMA colloidal crystal, it infiltrated the remaining voids

(44) Attard, G. S.; Glyde, J. C.; Goltner, C. G. *Nature* **1995**, *378*, 366−368.
(45) El-Safty, S. A.; Hanaoka, T. *Chem. Mater.* **2003**, *15*, 2892−2902.
(46) Xia, Y.; Mokaya, R. *Adv. Mater.* **2004**, *16*, 1553−1558.
(47) Xia, Y.; Yang, Z.; Mokaya, R. *J. Phys. Chem. B* **2004**, *108*, 19293−19298.
(48) Xia, Y.; Mokaya, R. *Chem. Mater.* **2005**, *17*, 1553−1560.
(49) Xia, Y.; Mokaya, R. *Adv. Mater.* **2004**, *16*, 886−891.
(50) Xia, Y.; Yang, Z.; Mokaya, R. *Chem. Mater.* **2006**, *18*, 140−148.
(51) Su, F.; Zeng, J.; Bao, X.; Yu, Y.; Lee, J. Y.; Zhao, X. S. *Chem. Mater.* **2005**, *17*, 3960−3967.
(52) Kyotani, T.; Nagai, T.; Inoue, S.; Tomita, A. *Chem. Mater.* **1997**, *9*, 609−615.
(53) Schroden, R. C.; Al-Daous, M.; Sokolov, S.; Melde, B. J.; Lytle, J. C.; Stein, A.; Carbajo, M. C.; Fernandez, J. T.; Rodriguez, E. E. *J. Mater. Chem.* **2002**, *12*, 3261−3327.

of the template by capillary forces. The completely infiltrated PMMA templates were heated in a vial covered with Parafilm at 45 °C for 22 h. Subsequently, they were calcined in air at 550 °C for 4 h (heating rate: 2 °C min^{-1}), to remove the PMMA and Brij 56. White monolithic pieces of 3DOM/m SiO_2 were obtained with typical bulk dimensions of ca. 0.8 × 0.6 × 0.2 cm^3.

Synthesis of 3DOM/m C Monoliths. Syntheses of 3DOM/m C monoliths were adapted from preparations of mesoporous carbon by Lee et al.[54,55] Before polymer infiltration, acidic sites were introduced into silica monoliths. As-synthesized 3DOM/m SiO_2 monoliths were immersed in a solution of 0.34 g of $AlCl_3 \cdot 6H_2O$ and 10 mL of DI water for 4 h at RT. Excess solution was removed by filtration. The monoliths were then dried in an oven at 80 °C overnight followed by calcination at 550 °C for 4 h with a heating rate of 1 °C·min^{-1}. These samples were denoted as 3DOM/m Al-SiO_2.

For a typical synthesis of 3DOM/m C, 0.182 g of 3DOM/m Al-SiO_2 monoliths, 0.273 g of phenol, and 0.174 g of paraformaldehyde were sealed in an Erlenmeyer flask with a glass valve. Care was taken that 3DOM/m Al-SiO_2 monoliths did not come into direct contact with phenol and paraformaldehyde powder. The flask was evacuated for 2 h before vapor-phase polymerization at 90 °C for 12 h. The phenolic resin−silica composite was heated with a heating rate of 1 °C·min^{-1} to 160 °C, held there for 5 h to stabilize the polymer, and then ramped at 5 °C·min^{-1} to 850 °C and carbonized for 7 h under nitrogen flow. Macro-/mesoporous carbon monoliths were obtained by removing silica with 10 wt % HF solution at RT for 24 h.[48] (CAUTION!! HF solution is extremely dangerous and corrosive and must be handled according to MSDS procedures.)

Synthesis of 3DOM/m C/C Nanocomposites. N-Doped graphite was introduced into the mesopores of 3DOM/m C monoliths by CVD with acetonitrile as the precursor.[46] 3DOM/m C monoliths were placed in a porcelain boat which was inserted into a quartz tube. High-purity nitrogen gas was bubbled through acetonitrile with a flow rate of ca. 20−50 mL·min^{-1} to form a saturated gas which passed through the quartz tube for 1 h at RT to purge the tube before the temperature was ramped to 1000 °C and maintained there for several hours. The sample was then cooled down to RT under pure nitrogen flow. Samples were named 3DOM/m C/C-*x*h, or abbreviated as CC-*x*h. For example, CC-2h means that the CVD reaction was carried out for 2 h.

As reference samples, 3DOM carbon monoliths without mesopores were synthesized from resorcinol and formaldehyde resin with PMMA monoliths as templates following a published procedure.[10] One modification of this procedure was the drying time of the exposed template−RF-sol composite in a convection oven at 85 °C after it had been aged in a sealed bottle at 85 °C for 3 days. This time was 1 h in the published procedure, 12 h for the sample named 3DOM RFC, and 0.5 h for the sample 3DOM RFC2.

Characterization. Powder X-ray diffraction (XRD) analysis was performed using a Bruker AXS microdiffractometer with a 2.2 kW sealed Cu X-ray source and a Hi-Star 2-D area detector. All diffraction patterns were acquired at a generator voltage of 45 kV and a current of 40 mA. For each measurement, small amounts of the powdered samples were attached to a piece of flat quartz, which was mounted on an aluminum stub. Small-angle X-ray scattering data were acquired on a Rigaku RU-200BVH 2-D SAXS instrument using a 12 kW rotating anode with a Cu source and a Siemens Hi-Star multiwire area detector. The sample-to-detector distances were 50 cm or 100 cm with exposure times of 100 s for each sample. The step interval was 0.01° 2θ. All samples were ground into fine powders before running tests. For 3DOM/m C/C monoliths, graphite chunks on the surface were removed by polishing with sandpaper before running SAXS and nitrogen-adsorption tests. Scanning electron microscopy (SEM) images were obtained with a JEOL 6700 scanning electron microscope at an accelerating voltage of 1.5 kV. Samples were mounted on an aluminum stub with conductive carbon sticky tape. For the nonconductive silica samples, a thin (ca. 5 nm) coating of platinum was deposited on the sample prior to analysis. Transmission electron microscopy (TEM) was conducted on a JEOL model JEM-1210 electron microscope that was operated at 120 kV. Samples for TEM measurements were drop-dried from ethanol onto a holey carbon film supported on a copper grid. C, H, O, and N elemental analyses (EA) of 3DOM carbon were performed by Atlantic Microlab Inc. of Norcross, GA. X-ray photoelectron spectroscopy was performed on a Kratos XSAM 800 instrument with an Al Kα X-ray anode operating at 200 W and a three-channel hemispherical electron energy analyzer. A background pressure of 10^{-9} Torr was maintained during XPS measurements. A path energy of 89.45 eV was used for a survey scan and 17.9 eV for a high-resolution scan. Raman spectroscopy was performed with a Spectra-Physics 2065-7S spectrometer with a 514.5 nm Ar-ion laser operating from 0.1 to 1 W. Signals were collected with a charge-coupled device (CCD) detector maintained at −120 °C. The instrument was calibrated with an indene standard of well-known peaks. A pressed pellet of graphite powder (Aldrich, <20 μm, synthetic) was used as a reference sample. All samples were in monolithic shapes and were mounted on glass microscope slides. A total of 32 scans were collected using an acquisition time of 30 s per scan. Thermogravimetric analysis (TGA) was carried out on a NETZSCH STA 409 instrument. Samples were heated in an alumina crucible under airflow from RT to 900 °C at a rate of 2 °C min^{-1}. Nitrogen-sorption measurements were performed on a Micromeritics ASAP 2000 gas sorptometer. Samples were degassed to 0.003 mmHg for 48 h at 120 °C. Specific surface areas were calculated by the Brunauer−Emmett−Teller (BET) method, and pore sizes and volumes were estimated from pore size distribution curves from the adsorption branches of the isotherms. Pore volumes were taken at the $P/P_0 = 0.985$ single point. Depth-sensing indentation (DSI) experiments were performed using an instrumented indenter (Nano Indenter XP, MTS Systems Corporation) with a diamond Berkovich indentation tip. The maximum load for each sample was 15−16 mN. Multiple load−unload cycles were conducted for each sample to examine the reproducibility.

Electrochemical Characterization. Galvanostatic charge−discharge measurements were performed with a two-electrode cell in which macroporous carbon monoliths were used as the working electrode and Li metal as the counter and reference electrodes. This electrode assembly was constructed in a dry room with <1% relative humidity and was contained in a three-necked glass round-bottomed flask. The flask was sealed with electrodes connected to their respective contacts with alligator clips. The electrolyte was 1.0 M $LiClO_4$ dissolved in propylene carbonate (PC). The separator (Celgard 2400, microporous polypropylene membrane) was purchased from Celgard, Inc.

Galvanostatic cycling experiments were conducted on an Arbin battery-testing system. For these experiments, various gravimetric currents were applied within a voltage range of 0.0−2.0 V (vs Li/Li^+). Applied currents increased from 0.05 to 5 mA with each cycle. The electrical conductivity of monolithic macroporous carbon was measured at room temperature via the 4 probe Van der Pauw method.[56] The probes were attached to the sample using Ag paste as an adhesive (Ted Pella).

(54) Lee, J.; Sohn, K.; Hyeon, T. *J. Am. Chem. Soc.* **2001**, *123*, 5146−5147.
(55) Lee, J.; Yoon, S.; Hyeon, T.; Oh, S. M.; Kim, K. B. *Chem. Commun.* **1999**, 2177−2178.

Figure 1. Photographs of samples taken after each processing stage. From left to right: 3DOM/m SiO_2 monoliths synthesized from PMMA colloidal crystal templates and PEO surfactants. 3DOM/m C obtained from 3DOM/m SiO_2 monolith after vapor-phase polymerization to introduce phenolic resin into mesopores, followed by carbonization and silica removal. 3DOM/m C/C nanocomposite monoliths, from chemical vapor deposition of N-doped graphite inside mesopores of 3DOM/m C. See text for details.

Table 1. BET Surface Area, Pore Diameter, and Total Pore Volume Data for Sample 3DOM/m SiO_2, 3DOM/M C, 3DOM/m C/C-2h, and 3DOM RFC

	S_{BET} ($m^2\ g^{-1}$) total/micropore	mesopore diameter (nm)	pore volume ($cm^3\ g^{-1}$) total/micropore	average macropore size[b] (nm)	average wall thickness[b] (nm)	density of monolith[c] ($g\ cm^{-3}$)	conductivity ($S\ cm^{-1}$)
3DOM/m SiO_2	1148/0	2.1	0.63/0	303 ± 5	26 ± 2	0.17	not applicable
3DOM/m C	1261/301	2.8	0.93/0.13	286 ± 2	38 ± 4	0.29	0.15
3DOM/m CC-2h	20/17	ND[a]	0.03/0.01	266 ± 5	58 ± 3	0.43	0.25
3DOM RFC	228/177	NA[d]	0.14/0.08	273 ± 8	18 ± 2	0.55	0.11
3DOM RFC2	342/277	NA[d]	0.19/0.13	360 ± 9	18 ± 2	0.33	0.25

[a] No mesopores were detected for 3DOM/m C/C-2h; see Figure 7(3). [b] Estimated from SEM images, Figures 2B, 2D, and 2E. [c] Densities were calculated from the mass of the same piece of monolith over its volume at different reaction stages: from 3DOM/m SiO_2 to 3DOM/m C and then to 3DOM/m CC-2h. Dimensions of the monolith were as follows: 0.80 × 0.60 × 0.2 cm^3. For 3DOM RFC, the dimensions were 1.0 × 0.8 × 0.2 cm^3. [d] Not applicable as the fraction of mesopores was small in this sample and mesopores were nonuniform.

Results and Discussion

Structure and Composition. The techniques employed in this study, gas-phase polymerization and chemical vapor deposition, have the advantage that they can replicate shapes of the original template (3DOM/m SiO_2 monolith) on both the macroscopic scale and the nanoscale. The photos in Figure 1 demonstrate that the external shape of the porous silica monolith was maintained throughout the complete 3D reproduction procedure. The starting monolith, 3DOM/m SiO_2, was noticeably opalescent, due to diffraction of visible light on the surface of the face-centered cubic skeleton. The porous carbon replica appeared to have lost most opalescence on the surface, possibly caused by excess carbon layers and fragments created during polymerization, carbonization, and HF etching. However, cross sections of the sample's interior showed visible opalescence, indicative of the highly periodic structure within the sample. Products obtained after CVD treatment were significantly heavier than the original 3DOM/m C monoliths (see the density values in Table 1) and they were mechanically more robust.

Scanning electron microscopy was used to monitor morphological changes after each reaction step. Corresponding images are shown in Figure 2. The monodisperse PMMA spheres synthesized by emulsifier-free emulsion polymerization formed colloidal crystal monoliths with FCC packing, which is typically observed after slow sedimentation and water evaporation.[57] As determined by image analysis from Figure 2A, the PMMA spheres have average diameters of 433 ± 5 nm. When these PMMA colloidal crystals were used as templates, 3DOM/m SiO_2 monoliths with macropores ca. 303 nm in diameter and pore windows ca. 100 nm in diameter were produced as a 3D-interconnected porous

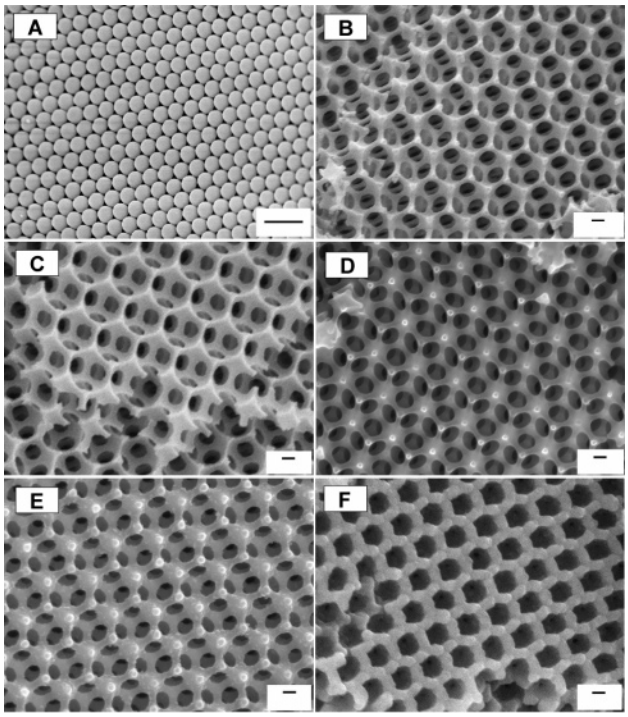

Figure 2. Scanning electron microscopy (SEM) images of samples at different processing stages: (A) PMMA colloidal crystal template. (B) 3DOM/m SiO_2 monolith synthesized with PMMA as template. (C) 3DOM/m Al-SiO_2 monolith, obtained from aluminum impregnation of the 3DOM/m SiO_2 monolith. (D) 3DOM/ m C, after introduction of polymer, carbonization, and removal of silica with HF. (E) CC-2h and (F) CC-5h carbon/graphite composite monoliths after CVD reaction times of 2 and 5 h, respectively. In (A), the scale bar is 1 μm and in the other images it is 100 nm.

(56) van der Pauw, L. J. *Philips Tech. Rev.* **1958/59**, *20*, 220−224.
(57) Zou, D.; Ma, S.; Guan, R.; Park, M.; Sun, L.; Aklonis, J. J.; Salovey, R. *J. Polym. Sci., Polym. Chem. Ed.* **1992**, *30*, 137−144.

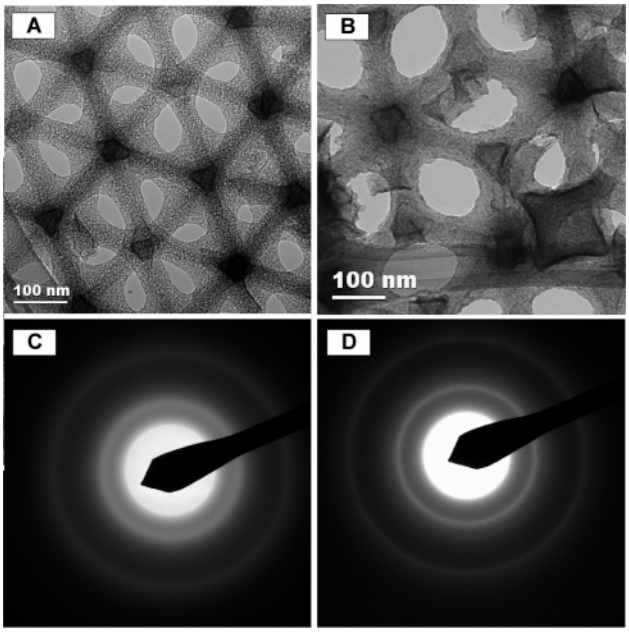

Figure 3. Transmission electron microscopy images of 3DOM/m C (A) and CC-2h (B). Corresponding selected-area electron diffraction patterns are shown in (C) and (D), respectively.

network was formed (Figure 2B). The observed pore shrinkage is typical for inverse opal oxides.[58,59] After Al impregnation to prepare the surface with acidic catalytic sites for vapor-phase polymerization of phenol formaldehyde, the 3DOM structure and dimensions did not change significantly (Figure 2C). The 3DOM/m C structures produced by nanocasting around the 3DOM/m SiO_2 template maintained the periodic, interconnected macropores of the template, while the walls were thicker than those of the template (Figure 2D). After CVD, growth of macropore walls and, after longer reaction times, a reduction in the diameters of pore windows was observed. Wall thicknesses increased moderately from 26 to 58 nm after 2-h CVD reaction, but window sizes were still ca. 100 nm (Figure 2E). With a longer deposition time (5 h), macropore wall thicknesses increased to 89 nm and pore windows were almost closed (Figure 2F). Detailed information about pore changes for 3DOM/m SiO_2, 3DOM/m C, and 3DOM/m C/C-2h is provided in Table 1. For comparison, 3DOM RFC templated directly from the PMMA colloidal crystal in Figure 2A had a macropore diameter of 273 nm and a much smaller average wall thickness of 18 nm, estimated from an SEM image (Figure S1 in Supporting Information).

More information about the macropore wall interior was obtained by transmission electron microscopy (TEM). Before the CVD reaction, the TEM image of 3DOM/m C showed smooth macropore wall surfaces and features typical for a wormlike mesopore structure (Figure 3A), in agreement with our conclusions from SAXS measurements. The interconnected wormlike pore structure provides good access to pores for subsequent filling with a second component. After infiltration of CVD carbon into the mesopores, wall thicknesses increased slightly, and a rougher surface was observed (Figure 3B), which may be due to some excess growth of carbon on the surface. Selected-area electron diffraction (SAED) displayed the difference more clearly. 3DOM/m C produced two broad diffraction rings due to its more amorphous nature (Figure 3C), while the composite material obtained after CVD (3DOM/m CC-2h) gave rise to two sharper rings (Figure 3D), indicative of greater order between graphene sheets.

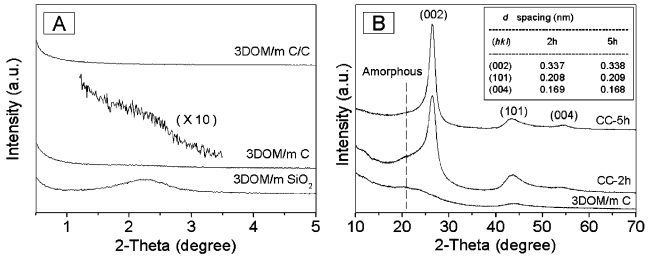

Figure 4. (A) Small-angle X-ray scattering (SAXS) and (B) powder X-ray diffraction patterns (XRD). In (A), the 3DOM/m C/C sample was obtained after 2 h of CVD. The pattern of 3DOM/m C between 1.2 and 3.5° 2θ was enlarged ten times so that the diffraction band at ca. 2.3° could be seen more clearly. In (B), the dashed line at ca. 22° 2θ indicates the position of a diffraction peak due to amorphous carbon. Calculated *d* spacing values of the (002), (101), and (004) reflections are displayed in the inserted table.

Small-angle X-ray scattering and powder X-ray diffraction revealed further information about the mesostructure and crystallinity of the materials. As shown in Figure 4A, 3DOM/m SiO_2 monoliths produced a broad peak at ca. 2.18° 2θ, which can be observed with a wormlike mesostructure with a pore spacing of 4.1 nm. Only a very weak reflection was seen in the same range for the 3DOM/m C monolith, indicative of even less regularity in the mesopore structure. After carbon infiltration by CVD, the 3DOM/m C/C monolith did not produce any low-angle peaks in the SAXS pattern. Filling of mesoporous carbon channels with more carbon eliminated scattering in the low-angle region by removing any electron density contrast between pore walls and filler material. Powder XRD yielded information about the carbon phases. In the wide-angle XRD pattern of 3DOM/m C (Figure 4B), only two weak and broad reflections were observed at ca. 22° and 44° 2θ, which could be attributed to turbostratic packing of graphene sheets in amorphous carbon.[60] After CVD with acetonitrile for 2 h, a sharp peak at ca. 27° 2θ was observed, together with two other relatively broad peaks, at ca. 44° and 55° 2θ. These peaks were assigned to diffraction from the (002), (101), and (004) planes of N-doped graphite.[46] While a weak reflection due to amorphous material was still observed as a shoulder at ca. 22°, the content of graphitic material was significantly higher in the nanocomposite materials. With a longer CVD time of 5 h, the (002) peak became narrower and more intense and the shoulder due to amorphous carbon almost disappeared, consistent with a higher loading of graphitic material. The *d*-spacings calculated from the (002) peak were 0.337 nm (2 h) and 0.338 nm (5 h), in agreement with reported values for graphite.[61]

(58) Schroden, R. C.; Al-Daous, M.; Blanford, C. F.; Stein, A. *Chem. Mater.* **2002**, *14*, 3305−3315.
(59) Yan, H.; Blanford, C. F.; Holland, B. T.; Smyrl, W. H.; Stein, A. *Chem. Mater.* **2000**, *12*, 1134−1141.
(60) Fricke, J.; Petricevic, R. In *Handbook of Porous Solids*; Schuth, F., Sing, K. S. W., Weitkamp, J., Eds.; Wiley-VCH: Weinheim, 2002; p 2037.

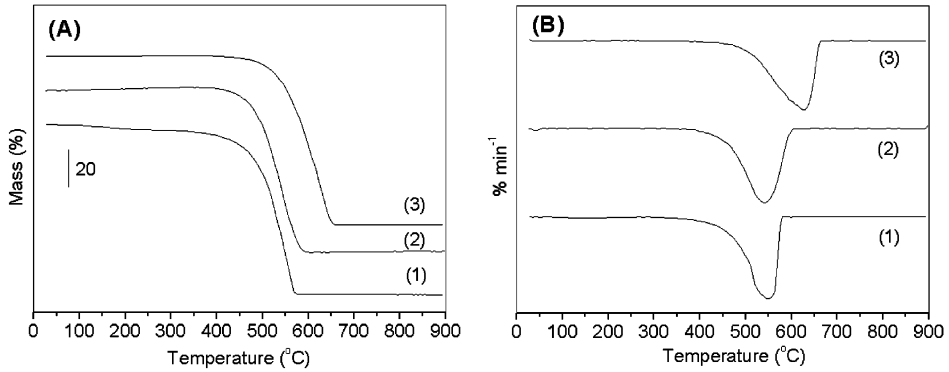

Figure 5. Thermogravimetric analysis (TGA) curves (A) and corresponding differential thermogravimetric (DTG) results (B) for (1) 3DOM RFC, (2) 3DOM/m C, and (3) 3DOM/m C/C-2h. Data traces are offset along the *y*-axes for easier comparison.

Raman spectra were obtained for 3DOM/m C, 3DOM/m C/C, 3DOM RFC, and graphite (Supporting Information, Figure S2). A peak was observed between 1598−1603 cm^{-1} for all three 3DOM samples and arose from the E_{2g} vibrational mode of graphite layers (G band).[10] This G band was much broader than the corresponding peak in the graphite reference sample at 1583 cm^{-1}. A broad peak at 1350 cm^{-1} for 3DOM/m C and 3DOM/m RFC was assigned to the disordered band (D band) of carbon, corresponding to turbostratic carbon layers or very small graphitic domains.[62] This peak shifted to 1363 cm^{-1} for 3DOM/m C/C. The peak pattern is similar to that reported for mesoporous carbon prepared by CVD[47,48] and for carbon aerogels.[60] The D/G peak intensity ratio of 3DOM/m C/C did not change significantly in comparison with 3DOM/m C and 3DOM RFC. The D band arises from the breakdown of the k-selection rule for small graphite domains, and its intensity is inversely proportional to the crystallite size.[62] The observed D/G intensity ratios were consistent with small graphitic domains confined inside mesoporous channels.

Thermogravimetric analysis is another suitable technique to probe the level of graphitization in carbon materials. As observed from the TGA traces in Figure 5A, 3DOM/m C is stable in air atmosphere up to ca. 420 °C, similar to 3DOM RFC. After incorporation of N-doped graphitic carbon by acetonitrile CVD for 2 h at 1000 °C, 3DOM/m C/C started combustion at a higher temperature of ca. 500 °C. Moreover, the combustion of 3DOM/m C/C was completed at ca. 650 °C, i.e., at a significantly higher temperature than for 3DOM RFC and 3DOM/m C (570−580 °C). Figure 5B shows differential thermogravimetric (DTG) traces calculated from the corresponding TGA curves. Peaks indicating mass loss events for 3DOM RFC and 3DOM/m C were centered around 549 and 538 °C, respectively. However, the corresponding peak for 3DOM/m C/C containing graphitic carbon was most intense at 624 °C, significantly higher than for the other two samples which were composed of amorphous carbon. Additionally, this peak for 3DOM/m C/C was more asymmetric, showing a shoulder in the range of 500−570 °C. This wide peak may be composed of two separate components, one from amorphous carbon and another from graphitic carbon. It can be concluded from these TGA data that the higher graphitic content in the carbon/carbon nanocomposite led to significantly improved thermal stability and combustion properties.

Surface compositions of 3DOM/m C and 3DOM/m C/C were analyzed by X-ray photoelectron spectroscopy (XPS). Scans were obtained at low and high resolution to provide a compositional overview and information about specific elements (C and N) (Figure 6). Both 3DOM/m C and C/C samples produced a strong C 1s peak between 282 and 289 eV. An oxygen 1s peak was also observed at 532.3 eV and attributed to oxygen-containing surface functional groups in carbon materials produced from oxygen-rich phenolic resins. A major difference between these two samples was a nitrogen 1s peak in the 3DOM/m C/C sample, a peak which was absent in the 3DOM/m C sample. This indicates that after CVD from acetonitrile, a significant amount of N was introduced into the monolith. Reconstruction of the carbon 1s peak was performed for the 3DOM/m C sample to reveal three components: the main carbon peak at 284.6 eV, a peak at 286.2 eV due to carbon atoms attached to hydroxyl or ether groups, and a third peak at 287.5 eV due to carbonyl or quinone groups.[63−66] Analysis of the C 1s region was similar for the CC-2h sample (not shown here). A high-resolution scan of the N 1s region of CC-2h revealed two peaks at 401.2 and 398.4 eV, which could be assigned to highly coordinated (quaternary) N atoms and pyridine-like N incorporated into graphitic sheets.[46]

Bulk compositions of the carbon samples were determined by elemental analysis (Table 2). Oxygen was introduced during the synthesis of 3DOM/m C via the oxygen-containing phenol−formaldehyde precursor. Chemisorption of moisture and CO_2 from the air may have contributed small amounts of additional oxygen.[67] After CVD of carbon at 1000 °C, nitrogen was introduced into the sample via the acetonitrile precursor, consistent with XPS data. Because the CVD reagent was oxygen-free, the relative fractions of carbon and

(61) Rodriguez-Reinoso, F.; Linares-Solano, A. In *Chemistry and Physics of Carbon*; Thrower, P. A., Ed.; Marcel Dekker, Inc.: New York, 1989; Vol. 21, pp 1−146.
(62) Tuinstra, F.; Koenig, J. L. *J. Chem. Phys.* **1970**, *53*, 1126−1130.
(63) Baker, W. S.; Long, J. W.; Stroud, R. M.; Rolison, D. R. *J. Non-Cryst. Solids* **2004**, *350*, 80−87.
(64) Boehm, H. P. *Carbon* **2002**, *40*, 145−149.
(65) Yue, Z. R.; Jiang, W.; Wang, L.; Gardner, S. D.; Pittman, C. U., Jr. *Carbon* **1999**, *37*, 1785−1796.
(66) Gardner, S. D.; Singamsetty, C. S. K.; Booth, G. L.; He, G.; Pittman, C. U., Jr. *Carbon* **1995**, *33*, 587−595.
(67) Wang, Z.; Ergang, S. N.; Al-Daous, A. M.; Stein, A. *Chem. Mater.* **2005**, *17*, 6805−6813.

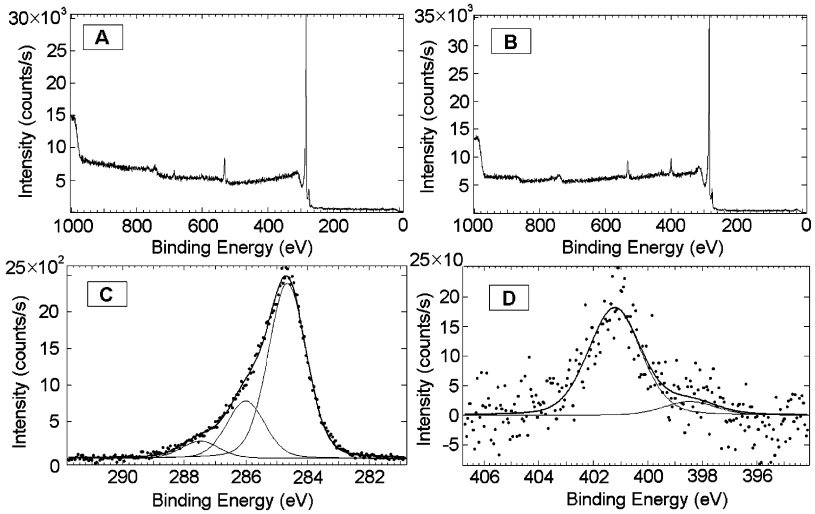

Figure 6. X-ray photoelectron spectra. Overviews for 3DOM/m C (A) and 3DOM/m C/C-2h (B) scanned at low resolution. High-resolution scans of carbon 1s (C) and nitrogen 1s (D) signals for 3DOM/m C/C-2h.

Table 2. Elemental Analyses of 3DOM/m C, CC-2h, and CC-5h[a]

	samples					
	3DOM/m C		CC-2h		CC-5h	
element	weight percent (%)	mole ratio	weight percent (%)	mole ratio	weight percent (%)	mole ratio
C	90.79	1.000	92.45	1.000	92.75	1.000
H	0.47	0.062	0.41	0.053	0.10	0.013
O	5.21	0.043	1.39	0.011	0.60	0.005
N	ND[a]	ND[b]	3.18	0.029	5.57	0.051

[a] All samples were ground into powder form and degassed at 200 °C for 6 h before analysis. [b] Nitrogen was not detected.

nitrogen increased with prolonged CVD treatment, while the relative proportions of hydrogen and oxygen in the samples decreased. Loss of oxygen-containing surface groups during the high-temperature treatment resulted in an additional reduction in the oxygen content of the CVD-treated samples.

To quantify porosity changes and evaluate the efficiency of infiltration, nitrogen-sorption analyses were performed (Figure 7 and Table 1). As-synthesized 3DOM SiO_2 monoliths showed a reversible type-IV adsorption isotherm as defined by IUPAC conventions (Figure 7A1).[68] This is similar to the HOM-*n* family of monolithic mesoporous silica reported by El-Safty and Hanaoka, which were synthesized from Brij 56 as surfactant.[45] However, members of the HOM-*n* family all have a mesopore size of 3 nm while 3DOM/m SiO_2 in this study contained pores with an average diameter of 2.1 nm. The replica, 3DOM/m C monolith, displayed a type-IV isotherm with an H2 hysteresis loop. A capillary condensation step into mesopores in the relative pressure (P/P_0) range of 0.4−0.9 was observed. This is typical for a CMK-3 carbon replica from ordered mesoporous silica templates.[29,46] A peak mesopore size of 2.9 nm was observed, but the pore-size distribution was broader than in the case of 3DOM/m SiO_2. The 3DOM/m C/C obtained after 2 h of CVD treatment with acetonitrile displayed a type-II isotherm, which is characteristic for macroporous materials. A small type-H3 hysteresis loop[69] was probably produced by surface defects or grain boundaries between amorphous carbon and N-doped graphite domains. No mesopores were detected in the pore size distribution curve for CC-2h. The isotherms for both carbon samples are very different from that reported for 3DOM RFC, which shows type II character with a type-H4 hysteresis due to the absence of uniform mesopores but significant microporosity.[10] Detailed analyses from nitrogen-adsorption measurements are listed in Table 1. After the conversion from 3DOM/m SiO_2 to 3DOM/m C, the surface area increased only slightly from 1148 to 1261 $m^2\ g^{-1}$, but decreased drastically after CVD infiltration to 20 $m^2\ g^{-1}$ (CC-2h) or 23 $m^2\ g^{-1}$ (CC-5h), both values near the theoretical value for 3DOM carbon with a smooth macropore wall surface and no micro- or mesopores. This indicates that most mesopores in MMC monolith were closed during chemical vapor deposition of graphite. The changes in pore volumes were consistent with those in BET surface areas: the 3DOM/m SiO_2 monolith had a total pore volume of 0.63 $cm^3\ g^{-1}$. Its replica, the 3DOM/m C monolith, exhibited a pore volume of 0.93 $cm^3\ g^{-1}$, which decreased to 0.03 $cm^3\ g^{-1}$ after graphite infiltration (for both CC-2h and CC-5h), confirming efficient filling of mesopores by the CVD method. The lower surface area observed for the 3DOM/m C/C samples is desirable in applications such as lithium-ion batteries. In these systems, formation of a solid-electrolyte-interface (SEI) layer is more extensive in high-surface-area electrodes, where it inhibits charge transport across the interface.

Mechanical Properties. Distinct qualitative differences in mechanical strength of the porous monoliths were noticed during handling of the samples. 3DOM RFC can be readily handled without breakage. It withstands light pressures, for example, during the preparation of a lithiation cell. Due to their high porosity, 3DOM/m C monoliths and their 3DOM/m SiO_2 preforms were more brittle than 3DOM RFC samples without templated mesopores. As noted before, 3DOM/m C/C products obtained after CVD treatment were mechanically more robust.

(68) Brunauer, S.; Deming, L. S.; Deming, W. S.; Teller, E. *J. Am. Chem. Soc.* **1940**, *62*, 1723−1732.

(69) Rouquerol, F.; Rouquerol, J.; Sing, K. *Adsorption by Powders and Porous Solids: Priciples, Methodology, Applications*; Academic Press: New York, 1999.

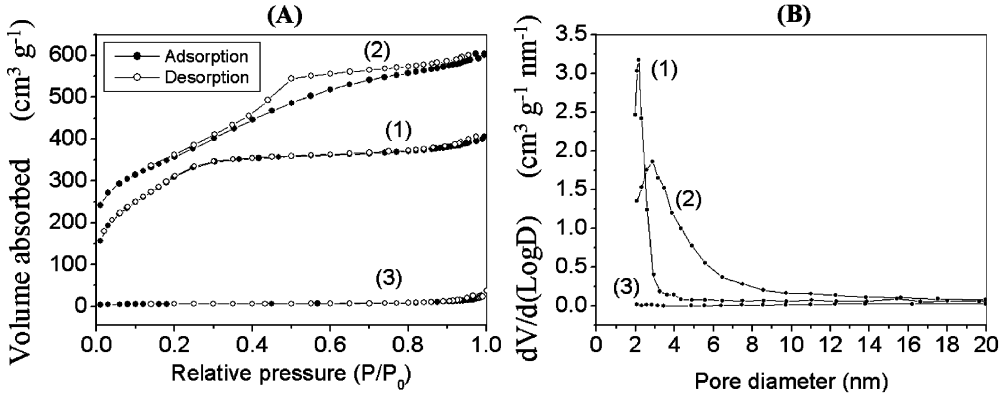

Figure 7. Nitrogen-sorption isotherms (A) and pore size distribution data (B): (1) 3DOM/m SiO_2 monolith; (2) 3DOM/m C monolith; (3) carbon/N-doped graphite composite monolith by 2 h of CVD (3DOM/m C/C-2h). Similar data for 3DOM RFC can be found in a previous publication.[10]

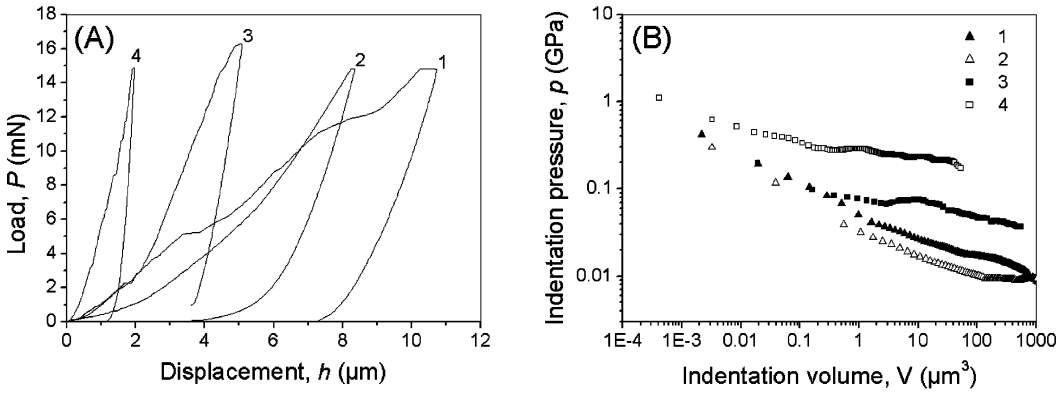

Figure 8. Indentation load−displacement ($P-h$) responses (A) and the plot of indentation contact response in pressure−volume ($p-V$) space for indentations made for a maximum load of 15−16 mN. Samples tested are (1) 3DOM/m SiO_2, (2) 3DOM/m C, (3) 3DOM/m C/C, and (4) 3DOM RFC.

To quantify this behavior, mechanical properties of the porous monoliths were tested by depth-sensing indentation (DSI) experiments. DSI measurements have previously been performed on 3DOM silica films on glass substrates and the deformation mechanism was discussed in detail.[70] In these experiments, contact loads are measured as a diamond Berkovich indentation tip with a trigonal pyramidal shape is lowered into the sample and then raised again (Figure S3). The resulting load−displacement traces can be used to quantify the mechanical integrity of the porous structures. Similar to the report for the published DSI study on 3DOM silica films, when multiple indentation measurements were carried out at different points of the porous monoliths, some scatter of data was observed. Differences in response likely resulted from positioning the tip near defects in the 3DOM structure. Multiple response curves are shown in the Supporting Information (Figure S4) and representative response curves of the porous monoliths (corresponding approximately to the median response for each sample) are compared in Figure 8A. At the same load of ca. 15 mN, the tip displacement followed the order 3DOM/m SiO_2 > 3DOM/m C > 3DOM/m C/C > 3DOM RFC. Notably, we observed a distinction between the 3DOM/m C/C monolith and the 3DOM/m C monolith, which was greater than the variations in $P-h$ responses. This indicates that the nanocomposite derived from 3DOM/m C after filling with graphitic carbon required a greater crushing pressure and thus had a higher resistance toward deformation. This improvement in mechanical strength was found to be vital for electrode applications, in particular for the lithiation of a monolithic electrode, in which the monolith was fixed in a cell between two clamped glass slides. Whereas 3DOM/m C did not withstand the pressure of this cell, 3DOM/m C/C samples were sufficiently strong for this purpose without needing any additional binder. 3DOM RFC showed the smallest displacement at the same load, indicating the highest resistance to crushing. This behavior is reasonable because the skeletal structure in 3DOM RFC was more continuous with fewer mesopores disrupting the wall. 3DOM/m C/C and 3DOM/m SiO_2 were weakened by mesopores in their walls. In the case of 3DOM/m C/C, although no mesopores were detected by nitrogen sorption measurements, incomplete filling was possible due to diffusion limitations during CVD, leaving some mesopores blocked by a graphitic coating.

In the previously reported study of supported 3DOM silica films, the indentation behavior was explained according to the following event sequence: (1) elastic deformation by cell-wall bending, (2) cell-wall fracture, (3) pore collapse, (4) local densification in a layer adjacent to the indenter face, and finally (5) compaction between the indenter.[70] For the samples studied here, contributions from mesopores and/or micropores should also be taken into consideration. In fact, the load−displacement curves show subtle features that may be interpreted in terms of response from pores vs pore walls. The traces are predominated by sloping lines, which indicate some elastic properties in the solid components (the walls

(70) Toivola, Y.; Stein, A.; Cook, F. R. *J. Mater. Res.* **2004**, *19*, 260−271.

and debris). In the case of 3DOM RFC and 3DOM/m C/C small horizontal steps with a step length of several hundred nanometers were seen in the $P-h$ curves. These horizontal step lengths are comparable to the size of macropores in these monoliths. For 3DOM/m SiO_2 and 3DOM/m C, small horizontal steps were not observed, even in multiple runs (Figure S4). A reason for this may be that the high porosity from disordered mesopores (and possibly micropores) in the macropore walls of these two samples reduced the differences between solid components and voids.

Modulus and hardness values obtained from standard load−displacement traces cannot be directly applied to these materials because of their nonelastic and nonvolume-conserving responses.[70,71] However, a material parameter could be derived from indentation pressure vs indentation volume plots to compare the "strength" of these porous materials. Indentation $P-h$ traces can be transformed into pressure−volume, $p-V$, traces through the shape of the Berkovich indenter profile at large contact depths according to the following relations:[70]

$$p = P/(24.5h^2)$$

$$V = (24.5h^3)/3$$

Figure 8B shows a plot of $p-V$ traces calculated from $P-h$ traces. Based on this plot, the monolith strength follows the order 3DOM RFC > 3DOM/m C/C > 3DOM/ m SiO_2 ≥ 3DOM/m C for all indentation volumes. Most importantly, filling mesopores with a graphitic phase strengthened the composite material (3DOM/m C/C) in comparison to its precursor (3DOM/m C).

Electrochemical Behavior. Recently, it has been shown that electrodes can benefit from the nanosize features and the bicontinuous pore/wall structure of the 3DOM architecture.[10−14] In the case of 3DOM carbon materials as anodes for lithium-ion batteries, for example, it has been demonstrated that much higher charging and discharging rates are possible than in nonporous carbon materials of identical composition and bulk dimensions.[10,72] 3DOM carbon produced from RF precursors was mainly amorphous (a hard carbon) and possessed moderate electronic conductivity (0.22 S cm^{-1}).[10]

The various structures prepared in this study allowed us to examine the effects of architecture and composition on conductivity, lithium-ion capacity, and charge/discharge rate behavior of the monolithic carbon pieces. In the context of comparing electronic conductivity, it should be noted that the conductivity of 3DOM RFC depends on synthesis conditions. The conductivity of the 3DOM RFC sample discussed above was 0.11 S cm^{-1}, i.e., half of the reported value.[10] For another sample, 3DOM RFC2, it was 0.25 S cm^{-1}. The different monoliths of 3DOM RFC were prepared as in a previous synthesis,[10] with one exception. After polymerization at 85 °C, 3DOM RFC was dried for 12 h at 85 °C in a convection oven, while 3DOM RFC2 was dried for only 30 min. The increase in drying time resulted in greater water loss through evaporation. As the water evaporates, it is believed that internal cracks develop and propagate through the material to ease the stress of the resin shrinkage. These internal cracks translate into the carbon structure after pyrolysis. Consequently, the overall conductivity of the monolith is reduced with the introduction of more grain boundaries. The comparison of conductivity values between 3DOM/m C and 3DOM/m C/C-2h is more straightforward, as the latter monolith was directly derived from the former. As might be expected for a sample containing a larger fraction of ordered carbon and thicker macropore walls, the electronic conductivity of 3DOM/m carbon increased by 67% from 0.15 to 0.25 S cm^{-1} after introduction of more graphitic carbon into the mesopores (Table 1). Thus, it is possible to tune electronic conductivity by formation of the amorphous carbon/graphitic carbon nanocomposite.

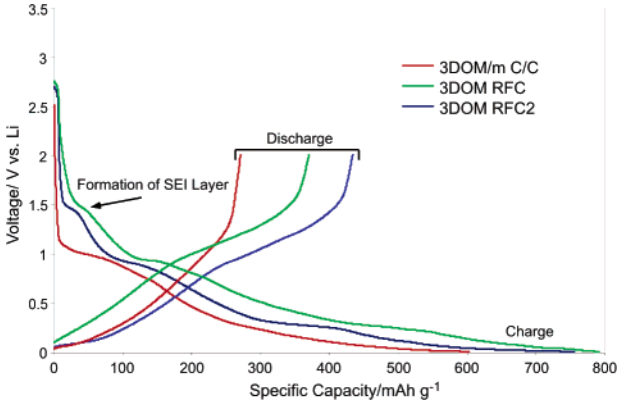

Figure 9. Specific charge and discharge capacities of 3DOM RFC, 3DOM RFC2, and 3DOM/m C/C.

As determined by galvanostatic cycling, the irreversible specific charge capacity for Li^+ of the 3DOM/m C/C monolith was 605 mA h g^{-1} compared to higher values of 792 and 758 mA h g^{-1} for 3DOM RFC and 3DOM RFC2, respectively (Figure 9). (3DOM/m C monoliths could not be tested due to limited mechanical strength.) The specific discharge capacities of these carbon monoliths were 272, 371, and 435 mA h g^{-1}, respectively. The theoretical capacity of graphite is 372 mA h g^{-1}, much less than that of hard carbon (theoretical value = 740 mA h g^{-1}),[73] and therefore the lower overall capacity of the nanocomposite at low rates is not completely unexpected. The increased specific charge capacity of the 3DOM RFC samples can also be attributed to the formation of a solid-electrolyte interface (SEI) layer on the C surface at 1.44 V vs Li/Li^+, which is apparent from the knee at this potential in the charge curves for the 3DOM RFC samples (Figure 9). The charging curve for 3DOM/m C/C did not show any evidence for development of an SEI layer at 1.44 V vs Li/Li^+. The SEI layer formation is dependent on the surface area of a carbon electrode and on the nature of the carbon itself.[74] A disordered hard carbon structure generates increased catalytic activity toward SEI layer formation, whereas the more ordered nature of the soft carbon graphene sheets leads to thinner SEI layers.[74]

(71) Oliver, W. C.; Pharr, G. M. *J. Mater. Res.* **1992**, *7*, 1564−1583.
(72) Take, H.; Kajii, H.; Yoshino, K. *Synth. Met.* **2001**, *121*, 1313−1314.
(73) Dahn, J. R.; Zheng, T.; Liu, Y.; Xue, J. S. *Science* **1995**, *270*, 590−593.
(74) Eshkenazi, V.; Peled, E.; Burstein, L.; Golodnitsky, D. *Solid State Ionics* **2004**, *170*, 83−89.

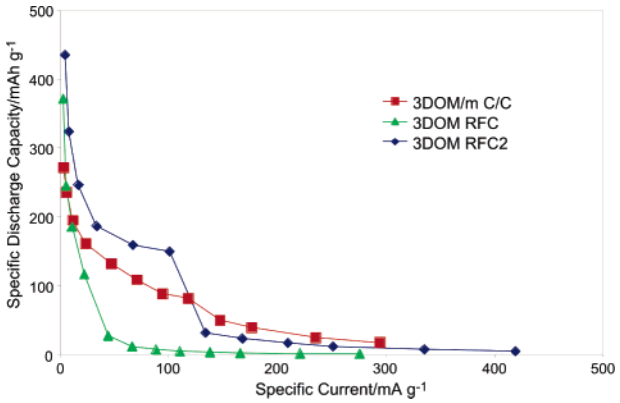

Figure 10. Specific discharge capacities of 3DOM RFC, 3DOM RFC2, and 3DOM/ m C/C.

3DOM/m C/C therefore has two advantages over the RFC samples: the coating of the macro-/mesoporous surface with soft carbon and the significantly reduced surface area of the hard carbon. Although the graphite grains are small, the increased order of the graphene sheets coupled with the significant surface area decrease seems to reduce the undesirable SEI layer formation.

Although the 3DOM/m C/C-2h monolith had the lowest reversible discharge capacity at low rates, it consistently maintained more capacity than either RFC sample when the discharge rate was increased (Figure 10). The lower surface area of the C/C material with a thinner SEI layer likely contributed to the increased rate capability. The lower conductivity and denser wall structure of 3DOM RFC both contribute to the poor rate capability of this material. 3DOM RFC2 maintained more capacity up to 120 mA h g^{-1}, but the presence of a thicker SEI layer on the microstructure likely resulted in the drop in discharge capacity at higher rates. Galvanostatic cycling results were consistent across multiple samples.

Conclusions

Nanocasting is a practical method to produce hierarchically structured carbon from silica templates with similar structural hierarchy. In a replication process based on gas-phase filling of mesopores with phenolic resin, followed by carbonization and silica removal, the structure is reproduced on multiple length scales. The product possesses mesopores, macropores, and bulk structure of a monolithic template. While it has previously been demonstrated that third-generation replica structures can be formed by multiple nanocasting (silica to carbon to silica after removal of carbon), this study has demonstrated that infiltration of a second carbon phase into porous replica carbon can result in products with significantly modified morphological, mechanical, electronic, and sorption properties.

Here, monolithic carbon/carbon nanocomposites with a hierarchical macroporous structure were synthesized by filling a 3D ordered macro-/mesoporous carbon monolith with N-doped graphitic carbon via CVD with acetonitrile as precursor. Interestingly, only mesopores were blocked or partially filled by this process, while macropores were left unaffected for short deposition times. The nanocomposite showed significantly improved graphitic order and thermal resistance to combustion in air, as compared with its amorphous template, macro-/mesoporous carbon. This graphitic component contains some nitrogen, as determined by XPS. The graphitic content in the nanocomposite and skeletal wall thickness could be controlled by the CVD time, both parameters increasing with longer deposition time. Mesoporosity also changed significantly during these processes. As monitored by nitrogen adsorption, the BET surface area decreased from >1200 m^2 g^{-1} for macro-/mesoporous carbon to 20 m^2 g^{-1} for the macroporous carbon/carbon nanocomposite after CVD treatment. This is a demonstration that CVD is an efficient and easy method to control surface porosity of biporous systems, as well as some of their physical properties. Depth-sensing indentation experiments revealed that the mechanical strength of a 3DOM/m C/C composite monolith was improved compared with 3DOM/m C, but 3DOM RFC monoliths without templated mesostructure in the wall were even stronger. Addition of a graphitic phase increased electronic conductivity of porous carbon, while lowering the capacity for lithium ions at low charge rates. Some advantages of the 3DOM/m C/C composite material in electrochemical experiments included a resistance toward forming a solid-electrolyte interface layer and greater lithium capacity at high charge and discharge rates, compared to 3DOM RFC with walls consisting only of amorphous carbon. Using carbon with hierarchical porosity as a basis for novel nanocomposites (including carbon and non-carbon guests within mesopores), it should be possible to fine-tune materials properties for a wide range of applications.

Acknowledgment. This research was supported by the Office of Naval Research (Grant No. N00014-01-1-0810, subcontracted from NWU), the Petroleum Research Foundation administered by the American Chemical Society (ACS-PRF Grant No. 42751-AC10), and in part by the MRSEC program of the NSF (DMR-0212302) which supports the University of Minnesota Characterization Facility. The authors thank Professor X. Zhu and Mr. Y. Deng for XPS measurements, Professor L. Que and Mr. J. Frisch for Raman measurements, Dr. J. Nelson for DSI measurements, and Professor W. H Smyrl for use of the electrochemical equipment.

Supporting Information Available: SEM image of 3DOM RFC, Raman spectra, schematic diagram of Berkovitch indenter, indentation load−displacement responses, and indentation contact response in pressure−volume space for multiple indentations. This material is available free of charge via the Internet at http://pubs.acs.org.

CM062050U